Journal of Nanobiotechnology

RESEARCH

Open Access

A thermo-sensitive hydrogel with prominent hemostatic effect prevents tumor recurrence via anti-anoikis-resistance

Yang Liu[1,2], Lei Ding[3,4], Gaojie Chen[1,2], Peiyuan Wang[5*] and Xinghuan Wang[1,2,6,7*]

Abstract

Tumor cells can survive when detached from the extracellular matrix (ECM) or lose cell–cell connections, a phenomenon known as anoikis-resistance (AR). AR is closely associated with tumor cell metastasis and recurrence, enabling tumor cells to disseminate, migrate, and invade after detachment. To address this issue, a novel intervention method combining intraoperative hemostasis with multifunctional nanozyme driven-enhanced chemodynamic therapy (ECDT) has been proposed, which holds the potential to weaken the AR capability of tumor cells and suppress tumor recurrence. Here, a nanocomposite containing a dendritic mesoporous nanoframework with Cu^{2+} was developed using an anion-assisted approach after surface PEG grafting and glucose oxidase (GOx) anchoring (DMSN-Cu@GOx/PEG). DMSN-Cu@GOx/PEG was further encapsulated in a thermal-sensitive hydrogel (H@DMSN-Cu@GOx/PEG). DMSN-Cu@GOx/PEG utilizes its high peroxidase (POD) activity to elevate intracellular ROS levels, thereby weakening the AR capability of bladder cancer cells. Additionally, through its excellent catalase (CAT) activity, DMSN-Cu@GOx/PEG converts the high level of hydrogen peroxide (H_2O_2) catalyzed by intracellular GOx into oxygen (O_2), effectively alleviating tumor hypoxia, downregulating hypoxia-inducible factor-1α (HIF-1α) expression, inhibiting epithelial-mesenchymal transition (EMT) processes, and ultimately suppressing the migration and invasion of bladder cancer cells. Interestingly, in vivo results showed that the thermosensitive hydrogel H@DMSN-Cu@GOx/PEG could rapidly gel at body temperature, forming a gel film on wounds to eliminate residual tumor tissue after tumor resection surgery. Importantly, H@DMSN-Cu@GOx/PEG exhibited excellent hemostatic capabilities, effectively enhancing tissue coagulation during post-tumor resection surgery and mitigating the risk of cancer cell dissemination and recurrence due to surgical bleeding. Such hydrogels undoubtedly possess strong surgical application. Our developed novel nanosystem and hydrogel can inhibit the AR capability of tumor cells and prevent recurrence post-surgery. This study represents the first report of using dendritic mesoporous silica-based nanoreactors for inhibiting the AR capability of bladder cancer cells and suppressing tumor recurrence post-surgery, providing a new avenue for developing strategies to impede tumor recurrence after surgery.

Keywords Hydrogel, Bladder cancer, Anoikis-resistance, Enhanced chemodynamic therapy, Hypoxia inducible factor-1α

*Correspondence:
Peiyuan Wang
wangpeiyuan@fjirsm.ac.cn
Xinghuan Wang
wangxinghuan@whu.edu.cn
Full list of author information is available at the end of the article

Graphical Abstract

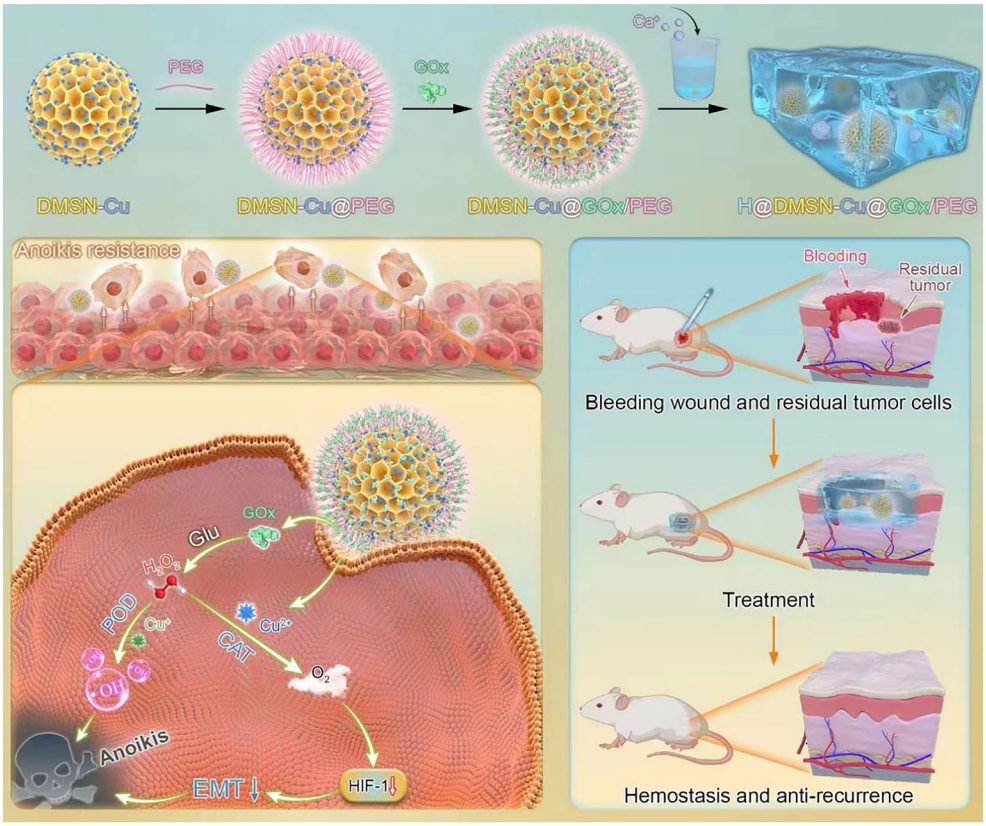

Introduction

Bladder cancer is one of the top ten most common cancers globally, with approximately 549,000 new cases and 200,000 deaths annually [1]. Non-muscle-invasive bladder cancer (NMIBC) accounts for about 75% of bladder cancer cases [2]. The primary treatment for NMIBC is transurethral resection of bladder tumor (TURBT); however, its postoperative recurrence rate remains high. Previous study has shown that NMIBC patients have an 80% recurrence rate within 5 years after TURBT, with 4–30% progressing to muscle-invasive bladder cancer (MIBC) [3]. Patients with MIBC often require radical cystectomy, which carries the risk of complete bladder removal. Therefore, it is crucial to inhibit postoperative recurrence in NMIBC patients and halt disease progression. Inadequate initial tumor resection and tumor residue after surgery are major reasons for high early recurrence rates in NMIBC patients [4]. The current armamentarium of postoperative adjuvant treatments, including radiation and chemotherapy, while essential, are fraught with limitations, including severe adverse effects and the potential for exacerbating patient morbidity [5]. Thus, our study emerges as a beacon of hope, introducing a novel therapeutic paradigm that transcends traditional modalities.

Anoikis-resistance (AR), a phenomenon wherein cancer cells defy the natural apoptotic response to detachment from the extracellular matrix (ECM), lies at the heart of metastatic dissemination and recurrence [6]. Following surgical intervention, circulating tumor cells, armed with AR, evade immune surveillance and establish secondary tumors [7]. Therefore, acquiring AR capability is an important early event and prerequisite for tumor metastasis and recurrence [6, 8].

Our study introduces a groundbreaking approach to tackling AR in bladder cancer by exploiting the tumor's reliance on reactive oxygen species (ROS) clearance for AR. By targeting the tumor's antioxidant defenses and inducing intracellular ROS accumulation, we aim to disrupt the AR mechanism [9]. Furthermore, considering the hypoxic tumor microenvironment (TME) as a hallmark of advanced solid tumors, our strategy also focuses on ameliorating hypoxia, a condition linked to tumor

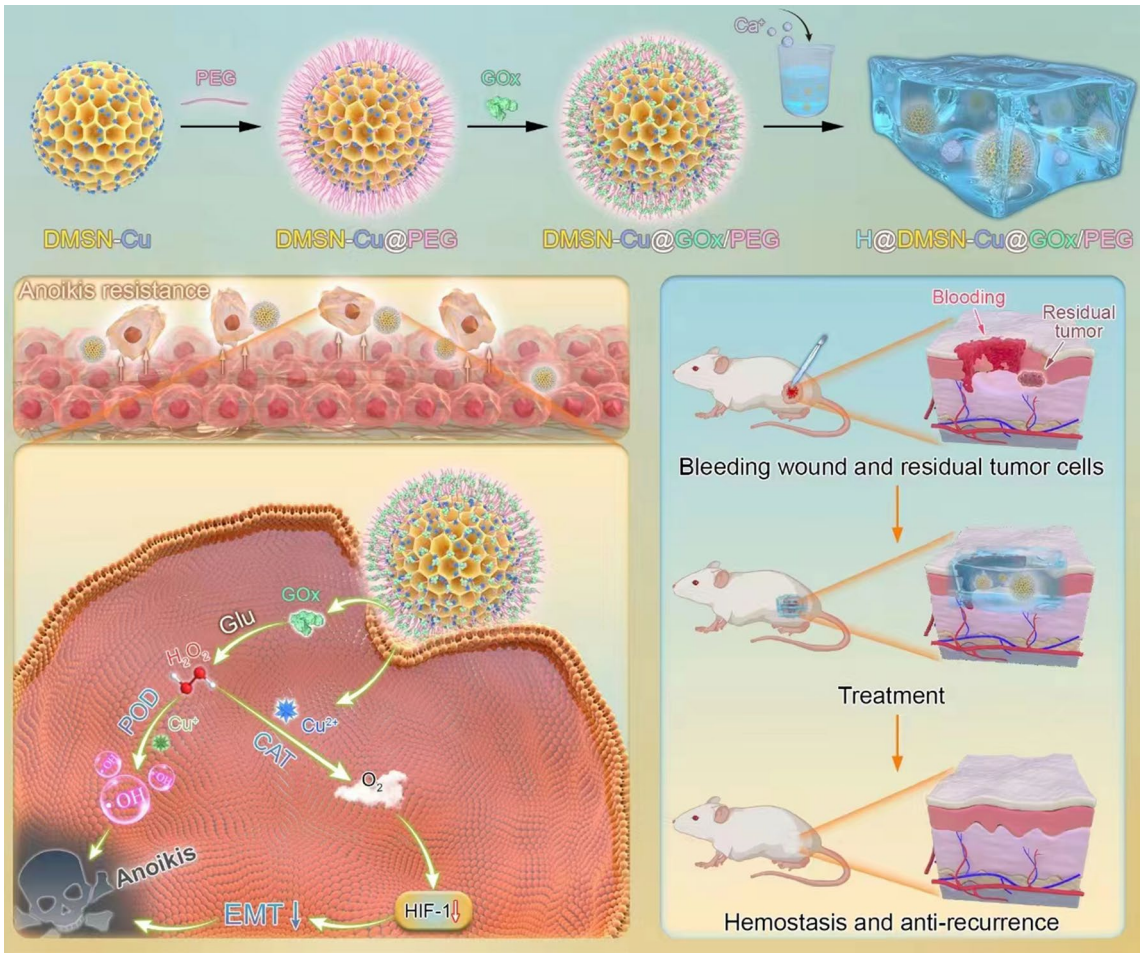

Scheme 1 Schematic illustration of stepwise fabrication of H@DMSN-Cu@GOx/PEG with excellent hemostatic properties for impeding tumor growth through the inhibition of anoikis-resistance (AR) via HIF-1/EMT disruption

aggression and poor prognosis [10–12]. Hypoxia promotes the stabilization of hypoxia-inducible factor-1α (HIF-1α), driving epithelial-mesenchymal transition (EMT), which facilitates tumor invasion and metastasis [10, 13]. EMT is crucial for the formation of highly invasive phenotypes in epithelial-derived stem cells, driving tumor metastasis and spread [14, 15]. EMT is integral to the AR of tumor cells, characterized by alterations in cadherin expression [16, 17]. Our objective is to harness these insights to design a therapeutic intervention that not only suppresses AR but also impedes tumor growth and dissemination.

In this work, we present the development of a copper(II)-incorporated dendritic mesoporous silica nanocarrier (DMSN-Cu@GOx/PEG) with dual peroxidase and catalase activities, facilitating enhanced chemodynamic therapy (ECDT) (scheme 1). This multifunctional nanoenzyme effectively targets bladder cancer cells with AR properties, elevates intracellular ROS levels, alleviates hypoxia by converting hydrogen peroxide to oxygen, downregulates HIF-1α, blocks EMT, and consequently restrains tumor recurrence and metastasis. To optimize local drug delivery and minimize systemic toxicity, we integrate DMSN-Cu@GOx/PEG into a thermosensitive hydrogel composed of Pluronic F127 (F127) [18] and calcium ions (H@DMSN-Cu@GOx/PEG) [19, 20]. Owing to calcium ions loading, H@DMSN-Cu@GOx/PEG exhibits excellent hemostatic capabilities, effectively enhancing tissue coagulation post-tumor resection surgery [21]. This formulation ensures sustained release and direct action at the tumor site, with the added benefit of hemostasis post-resection. The hydrogel rapidly solidifies at body temperature, forming a protective barrier that eradicates residual tumor tissue through ECDT-driven by the multifunctional nanoenzyme. With its dual capabilities of promoting tissue coagulation and combating tumor recurrence, H@DMSN-Cu@GOx/PEG offers a novel paradigm for bladder cancer postoperative care

and the inhibition of AR, potentially revolutionizing the field of bladder cancer therapy.

Materials and methods

Materials

$Cu(NO_3)_2$ was purchased from Aladdin Industrial Inc. Bis[3-(triethoxysilyl)propyl] tetrasulfide (BTES), Cetyltrimethylammonium p-toluenesulfonate (CTAT), 3,3,5,5′-Tetramethylbenzidine (TMB), Hexamethylenetetramine and F127 were obtained for Sigma-Aldrich. Ethanol, NaOH, cyclohexane and NH_4NO_3 were obtained from Shanghai Chemical Co., Ltd. Ammonia aqueous solution (28 wt %), tetraethyl orthosilicate (TEOS), triethanolamine (TEA) was purchased from Aladdin Industrial Inc. Glucose oxidase (GOx) and PEG_{2000}-NH_2 were obtained from Shanghai Yisheng Biotechnology Inc. Hydrogen Peroxide Assay Kit was bought from Shanghai Beyotime Biotechnology Inc. All chemicals were used as received without any further purification.

Synthesis of DMSN-Cu@GOx/PEG and H@DMSN-Cu@GOx/PEG

DMSN-Cu synthesis: Cu^{2+} incorporated dendritic mesoporous silica nanoparticles with tetrasulfide bond doping (DMSN-Cu) were fabricated as follows. Typically, TEA (0.034 g) and CTAT (240 mg) were concurrently added to deionized water (11.5 mL). After ultra-sounded for 0.5 h at room temperature and gently stirred at oil bath at 80 ℃ for another 0.5 h, then, 10 mg of $Cu(NO_3)_2$ dissolved in 1 mL of deionized water, a 1 mL of tetraethyl orthosilicate (TEOS) and 0.8 mL of and 1,2-bis(triethoxysilyl)-ethane (BTES) mixed solution was subsequently added to above water/CTAT/TEA solution with continuous stirring for 16 h. The fabricated mesoporous products were isolated by a high-speed centrifugation (10,000 rpm, 10 min), washed 3 times with ethanol and water in sequence and dried at 60 ℃ under a vacuum for 12 h. To remove the excess CTAT, 50 mg of DMSN-Cu were added in 60 mL, 5 mg/mL of NH_4NO_3/ethanol solution and refluxed overnight at 45 ℃. After repeated 4 times before thoroughly washed by ethanol and water in sequence. The final products were dried at 60 ℃ under a vacuum for 12 h.

Fabrication of DMSN-Cu@PEG: A mixed aqueous solution (5 mL deionized water) containing 10 mg of DMSN-Cu and 25 mg of PEG_{2000}-NH_2 was magnetically stirred at 37 ℃ for 24 h. Subsequently, the precipitate was separated by a high-speed centrifugation (10,000 rpm, 10 min). The as-made mesoporous product re-dispersed in deionized water were mediate for 5 min using a vortex analyzer. In order to remove the excessive PEG_{2000}-NH_2, DMSN-Cu@PEG was washed 4 times by deionized water (10,000 rpm, 10 min). The final collected DMSN-Cu@PEG precipitate was finally dried by a vacuum overnight, DMSN-Cu@PEG was stored at 4 ℃ for further modification.

Construction of DMSN-Cu@GOx/PEG: a mixed phosphate buffered saline (PBS; 1X, 10 mL, pH = 7.4) solution containing 20 mg of N-(3-dimethylaminopropyl)-N′-ethylcarbodiimide hydrochloride (EDC), 20 mg of N-hydroxysuccinimide (NHS) and 10 mg of GOx was magnetically stirred for 2 h, latter, above prepared DMSN-Cu@PEG was introduced to above mixed system and kept gent stirring for more than 12 h at room temperature. Immediately, the prepared DMSN-Cu@GOx/PEG was obtained by a high-speed centrifugation (10,000 rpm, 5 min) followed by 3 times washing via deionized water. Finally, the GOx encapsulated dendritic nanocomposite was stored at 4 ℃.

Construction of H@DMSN-Cu@GOx/PEG: For the hydrogel loading DMSN-Cu@GOx/PEG preparation, briefly, 2 g 20% (w/w) of F127 and 40 mg 0.4%(w/w) of $CaCl_2$ were dissolved in 10 mL of PBS (1X, 0.01 M, pH 7.4) under magnetically string at 4 ℃ for 12 h when the F127 hydrogel can be formed with Ca^{2+} loading. For nanoplatform loading,500 mg 5% (w/w) of DMSN-Cu@GOx/PEG powder was gradually added to the above F127-Ca^{2+} hydrogel to make a homogenous and monodisperse mixture with continuous stirring at 4 ℃ for 12 h After complete gel formation, the final H@DMSN-Cu@GOx/PEG spray was kept at 4 ℃.

Characterization of DMSN-Cu@GOx

The morphologies of nanoparticles were observed with a LEO1530VP SEM (Germany), a JEOL JEM2100 TEM (Japan), a Bruker Multimode 8, high-resolution transmission electron microscope operating at 200 kV. The UV–vis-NIR absorption spectra were performed on an Agilent Cary 5000 UV/vis/NIR spectrometer (USA). The chemical properties were characterized by the FTIR spectroscopy (Thermo Nicolet is50). The hydrodynamic diameter and Zeta potential were recorded with a Brookhaven Omni (U.K.). The N_2 adsorption/desorption branch of the isotherms were detected by a Quantachrome Autosorb iQ2. The confocal images were acquired on a Leica TCS SP5 CLSM (Germany).

Detection of colloidal stability: DMSN-Cu@GOx/PEG nanoparticles were dispersed in culture medium containing 10% FBS, and changes in average particle size and polydispersity index (PDI) within 7 days were monitored using a particle size analyzer.

Detection of POD activity: Using 3,3′,5,5′-tetramethylbenzidine (TMB) as a substrate in the presence of hydrogen peroxide, the POD-like activity of DMSN-Cu@GOx/PEG was evaluated. UV–Vis spectrophotometry was used to record the absorbance of the color reaction at

specific reaction times. In a 1 mL PBS solution (pH = 5.5) containing H_2O_2 (10 mM), TMB solution (0.1 mg/mL) was added followed by DMSN@PEG, DMSN-Cu@PEG, DMSN-Cu@GOx/PEG, and DMSN-Cu@GOx/PEG+Glucose (0.1 mg/mL). The absorbance changes of the color reaction were recorded using UV–Vis spectrophotometry at room temperature after a certain reaction time.

Detection of CAT activity: DMSN@PEG, DMSN-Cu@PEG, DMSN-Cu@GOx/PEG, and DMSN-Cu@GOx/PEG+Glucose (0.1 mg/mL) solutions were prepared using degassed PBS. The dissolved oxygen probe (AR8010, SMART SENSOR, China) was immersed in the solution, and after stabilizing the dissolved oxygen meter reading, hydrogen peroxide (final concentration 10 mM) was added. Real-time changes in dissolved oxygen concentration were monitored.

Cell culture

Bladder cancer cell line-T24 cells were kindly provided by the Cell Bank of the Chinese Academy of Science (Shanghai, China). In the cultivation of T24 cells, 100 U mL^{-1} of penicillin (Invitrogen, Shanghai, China), 10% fetal bovine serum (Invitrogen, Shanghai, China), and 0.1 g mL^{-1} streptomycin sulfate were added to RPMI 1640 medium (Invitrogen, Shanghai, China). All cells were incubated under an atmosphere with 5% CO_2 at 37 ℃.

Construction of AR-bladder cancer cell model

T24 cells were seeded onto suspension culture plates and subjected to standard cultivation procedures, involving medium replacement every 2 days, for an uninterrupted suspension culture duration of 7 days. Subsequently, cells were regularly harvested through enzymatic digestion and subsequently subcultured onto conventional cell culture plates. The cells demonstrating the ability to reattach and subsequently proliferate were identified as displaying resistance to anoikis and were consequently selected for subsequent experiment.

Cell viability assay

T24 cells were cultured in a 24-well plate for 24 h. DMSN@PEG, DMSN-Cu@PEG or DMSN-Cu@GOx/PEG was gently introduced into each well, and after co-incubation with the cells for 12 h, cell viability was assessed using the CCK-8 assay. Live/dead cell toxicity assessments were conducted with a commercially available assay kit (Calcein/PI Live/dead Viability/cytotoxicity assay kit, Beyotime Biotechnology), and images were captured using a confocal fluorescence microscope (Nikon, C2, Japan).

Intracellular ROS production

The DCFH-DA probe was employed to assess intracellular ROS generation. 5×10^4 T24 cells were seeded in each well of a 6-well plate. Subsequently, DMSN@PEG, DMSN-Cu@PEG, or DMSN-Cu@GOx/PEG were added to the cells, followed by a 24-h co-incubation. Afterward, the cells were stained with 50 μM DCFH-DA for 30 min and washed with PBS buffer. Finally, cell analysis was promptly carried out using a flow cytometer (BD LSRFortessa™X-20).

Detection of mitochondrial membrane potential (MMP)

The assessment of MMP in T24 cells was performed using the JC-1 assay kit (Multisciences, Hangzhou, China) following the manufacturer's protocol. In brief, T24 cells were seeded in a 6-well plate and treated with DMSN@PEG, DMSN-Cu@PEG, or DMSN-Cu@GOx/PEG for 24 h. Subsequently, the cells were incubated at 37 ℃ with 1 mL of JC-1 working solution for 20 min. Finally, immediate cell analysis was conducted using a flow cytometer (BD LSRFortessa™X-20).

Western blotting

Protease inhibitors were incorporated into RIPA buffer (Beyotime, Shanghai, China) to ensure protein extraction while cells were lysed on ice. The protein was subjected to electrophoresis on an 8–15% sodium dodecyl sulfate–polyacrylamide gel (SDS-PAGE) and subsequently transferred to a polyvinylidene difluoride (PVDF) membrane (Sigma Aldrich, Shanghai, China). The membrane was sealed with blocking buffer (Servicebio, Wuhan, China) for 15 min. The PVDF membrane was then incubated with the designated primary antibody at 4 ℃ overnight. Following washing with Tris buffer saline with tween 20 (TBST), the PVDF membrane and corresponding secondary antibodies were incubated at room temperature for 1 h. Imaging of the PVDF membrane was visualized by fluorescence chemiluminescence gel imaging system (Tanon 5200, Wuhan, China).

Anti-tumor effect of hydrogel in vivo

A tumor model was established by subcutaneously injecting T24 cells into the right hind flank of nude Balb/c mice. When the tumor volume reached approximately 100 mm^3, 25 nude mice were randomly divided into five groups: (1) Control group, received no treatment; (2) Tumor-bearing mice with tumor resection only; (3) Tumor-bearing mice underwent tumor resection followed by postoperative treatment with H@DMSN@PEG; (4) Tumor-bearing mice underwent tumor resection followed by postoperative treatment with H@DMSN-Cu@PEG; (5) Tumor-bearing mice underwent tumor

resection followed by postoperative treatment with H@DMSN-Cu@GOx/PEG. For mice with resected tumors, a skin incision was made along the tumor margin after anesthesia, and the tumor mass was excised along the tumor boundary and normal tissue. The surgical wound was routinely sutured and covered with antibiotic ointment to prevent postoperative infection. Groups (3) to (5) had the entire wound covered with H@DMSN@PEG, H@DMSN-Cu@PEG, and H@DMSN-Cu@GOx/PEG, respectively. The tumor volume in nude mice was assessed at 3-day intervals and computed using the formula: Volume = (width^2 × length) × 0.52. The animal study protocol adhered to the guidelines outlined in the "Guide for the Care and Use of Laboratory Animals" by the Association for Assessment and Accreditation of Laboratory Animal Care. Additionally, it received approval from the *Institutional Animal Care and Use Committee* of Wuhan University (Approval No. WP20230223).

Evaluation of cytocompatibility of hydrogels

A suspension of mouse fibroblast-L929 cells (200 μL, 5×10^4 cells mL^{-1}) was introduced into a 96-well microplate and incubated for 24 h. Subsequently, 10 μL of hydrogel or PBS was added to the respective groups, and they were further cultured for 72 h. Cell viability was assessed using the CCK-8 method. The viability and cytotoxicity of the cells were determined utilizing a commercially available assay kit (Calcein/PI Live/dead Viability/cytotoxicity assay kit, Beyotime Biotechnology), and images were captured using a confocal fluorescence microscope (Nikon, C2, Japan).

In vivo toxicity detection

Twenty male BALB/c-nude mice (6 weeks-old) were randomly assigned to four groups: Control, H@DMSN@PEG, H@DMSN-Cu@PEG, and H@DMSN-Cu@GOx/PEG. The mice were anesthetized with sodium pentobarbital (1%, 5 μL g^-1) and administered 10 μL of hydrogel intraperitoneally. One week later, the mice were euthanized, and their hearts, livers, spleens, lungs, and kidneys were harvested. Tissues were fixed in 4% formaldehyde for 24 h, followed by embedding, sectioning, and H&E staining. Histological analysis was conducted by three pathologists.

Blood clotting evaluation

Commercial gelatin sponge, H@DMSN@PEG, H@DMSN-Cu@PEG and H@DMSN-Cu@GOx/PEG were placed in centrifuge tubes. Subsequently, 50 μL of anticoagulant mouse blood was applied to the surfaces of the samples, and 5 μL of 0.2 M $CaCl_2$ solution was added. After a 1-min incubation, 10 mL of deionized water was added to dissolve hemoglobin without disturbing the blood clot. The absorbance of distilled water at 540 nm was determined using UV–visible spectrophotometry, with the absorbance of 10 mL of water mixed with 50 μL of anticoagulant mouse blood solution serving as the reference value. The Blood Clotting Index (BCI) was defined as BCI (%) = AS/AR × 100%, where AS represents the absorbance of distilled water in the sample group, and AR is the absorbance of the reference group.

In vivo liver hemostasis assay

C57BL/6 J male mice (6 weeks-old) were anesthetized using a 1% sodium pentobarbital solution. A laparotomy was performed to fully expose the liver within the abdominal cavity. A surgical incision, measuring approximately 0.2 × 0.2 cm, was created on the surface of the liver. A 0.2 cm-wide indicator strip made from filter paper was prepared, and a black reference line was drawn 0.5 cm from the end of the strip. Following the initiation of bleeding from the incision, the indicator strip was immediately placed on the wound. Subsequently, blood seeped along the indicator strip. If blood reached the black line within 3 s, it indicated that the bleeding rate and initial volume met the requirements for subsequent hemostasis experiments. After hemostasis assessment, an equivalent amount of hydrogel or medical gauze was applied to the wound for a hemostasis experiment. In the blank control group, only the incision was created without any hemostatic treatment. Intermittent assessments of active bleeding from the wound were made using the indicator strip. If there was no noticeable blood penetration along the indicator strip, it signified the absence of active bleeding. The total bleeding time was recorded. Following the conclusion of the hemostasis experiment, the abdominal cavity was rinsed with 10 mL of saline. The absorbance of the peritoneal lavage fluid was determined using a microplate reader (EnVision Xcite, PerkinElmer) to indirectly evaluate the amount of bleeding.

Statistical analysis

The analyzed experimental results were derived from a minimum of three independently replicated experiments. Data analysis and visualization were performed using GraphPad Prism 8.0 and SPSS (IBM, version 21.0). All data are expressed as mean ± standard deviation (SD). To assess differences between groups, we employed either a two-tailed Student's t-test or one-way analysis of variance (ANOVA). A significance level of $P < 0.05$ was considered significant, and $P < 0.01$ was regarded as highly significant.

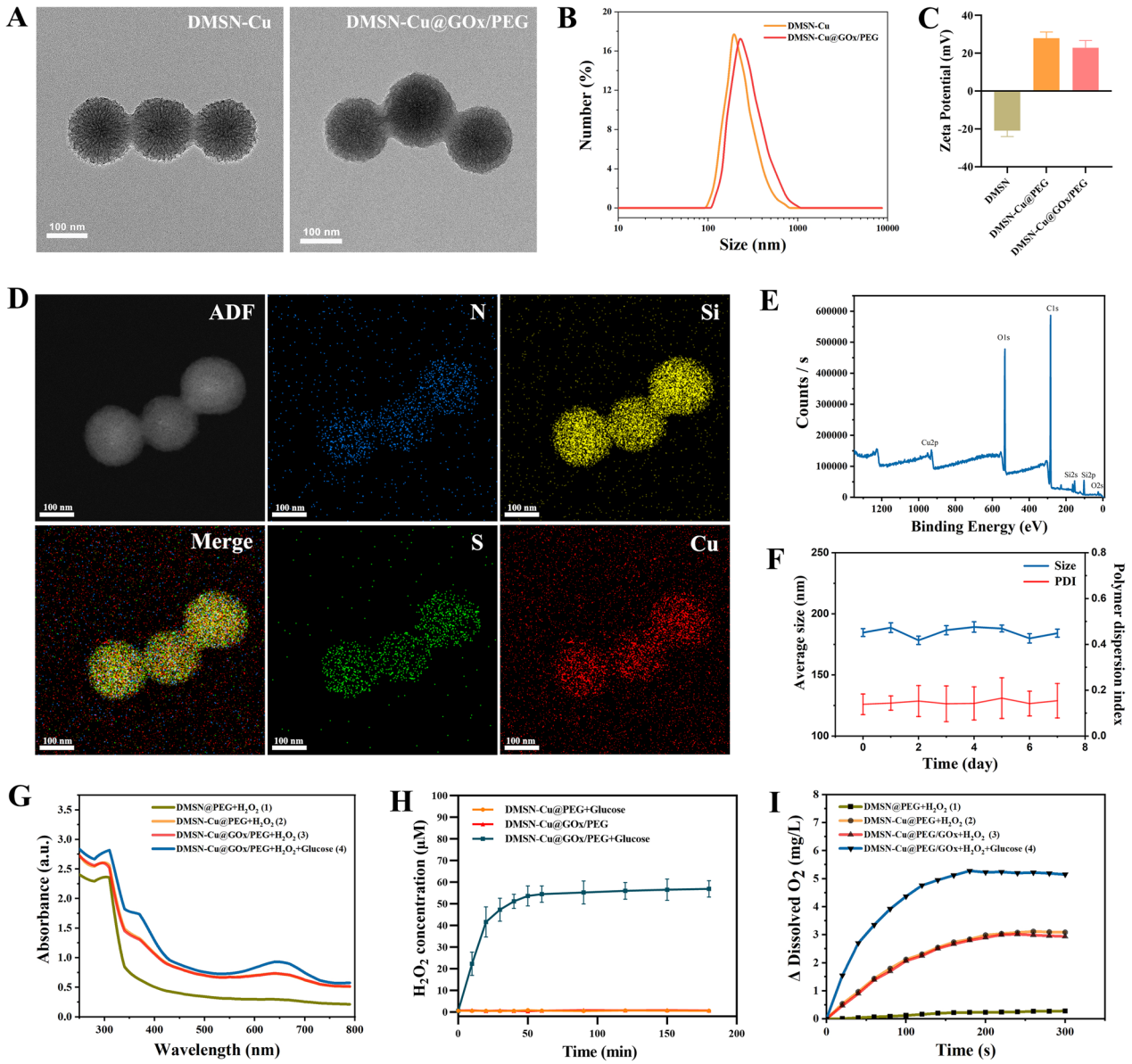

Fig. 1 Characterization and properties of nanoparticles. **A** TEM image of DMSN-Cu and DMSN-Cu@GOx/PEG. **B** The DLS of DMSN-Cu and DMSN-Cu@GOx/PEG. **C** The surface zeta potential of the DMSN, DMSN-Cu@PEG and DMSN-Cu@GOx/PEG (n = 3). **D** HAADF-STEM image and the corresponding element mapping images of DMSN-Cu@GOx/PEG. **E** XPS spectrum of DMSN-Cu@GOx/PEG. **F** Average size and PDI of DMSN-Cu@GOx/PEG after storage at room temperature for 1 week, respectively. The data was obtained from DLS. Data are presented as mean ± S.D (n = 3). **G** UV–vis absorption spectra of the catalyzed oxidation of TMB as catalyzed by: (1) DMSN@PEG + H_2O_2; (2) DMSN-Cu@PEG + H_2O_2; (3) DMSN-Cu@GOx/PEG + H_2O_2; (4) DMSN-Cu@GOx/PEG + H_2O_2 + Glucose in an acid environment (pH = 5.5). **H** H_2O_2 production in different groups (n = 3). **I** Oxygen release profiles of different groups

Results and discussion

Synthesis and characterization of DMSN-Cu@GOx/PEG

As shown in Fig. 1A, the images of Transmission electron microscopy (TEM) demonstrated that DMSN-Cu exhibited a uniform spherical mesoporous structure. Subsequently, a dense layer of PEG2000-NH_2 was applied to enhance circulation time and bioavailability, facilitating subsequent modifications. GOx was then covalently bound to DMSN-Cu@PEG via an EDC/NHS reaction. TEM images of DMSN-Cu@GOx/PEG confirmed the presence of a distinct PEG coating, indicating successful material synthesis. Dynamic light scattering (DLS) analysis (Fig. 1B) revealed that the hydrodynamic diameter (Dh) of DMSN-Cu is approximately 190.137 nm.

Following GOx and PEG coating, the Dh of nano-particles exhibited minimal change. Zeta potential measurements (Fig. 1C) showed an increase from − 20.9 mV to 27.9 mV and 22.9 mV for DMSN-Cu@PEG and DMSN-Cu@GOx/PEG, respectively. Fourier transform infrared spectrometer (FTIR) data of DMSN-Cu@GOx/PEG also demonstrated that peaks at 1235 cm^{-1} and 1050 cm^{-1} should be assigned to alcoholic hydroxyl and phenolic hydroxyl group from PEG_{2000}-NH_2 and tyrosine in GOx (Fig. S2). All avove findings indicated the successful PEG_{2000}-NH_2 modification and GOx loading. Further, elemental mapping and energy-dispersive X-ray spectroscopy (EDS) confirmed uniform distribution of N, Si, S, Cu, validating successful Cu^{2+} incorporation within DMSN-Cu@GOx/PEG. X-ray photoelectron spectroscopy (XPS) (Fig. 1E) revealed characteristic Cu 2p peaks at 934.8 eV (2p2/3) and 954 eV (2p1/2), confirming Cu^{2+} integration into the silica nanoframework.

Moreover, N_2 adsorption/desorption isotherms at 77 K (Fig. S3) indicated a specific surface area of approximately ~ 543.2 m^2 g^{-1} for DMSN-Cu, with dendritic mesopores ranging from 0.2 to 12.5 nm in diameter, crucial for cargo delivery efficiency. Furthermore, MSN-Ce@SP/PEG dispersion in cell culture media and 10% FBS showed consistent Dh and polymer dispersity index (PDI) over 7 days (Fig. 1F), demonstrating excellent stability of DMSN-Cu@GOx/PEG under physiological conditions. Subsequently, we investigated the in vitro chemodynamic property of DMSN-Cu@GOx/PEG. Using TMB as a •OH detection probe (Fig. 1G), we observed that under acidic conditions, DMSN-Cu@PEG and DMSN-Cu@GOx/PEG exhibited catalytic toxicity towards H_2O_2 production, in contrast to DMSN@PEG. The ability of DMSN-Cu@GOx/PEG to generate ·OH was likely due to GOx catalyzing glucose substrate into H_2O_2, confirmed by hydrogen peroxide assay (Fig. 1H). Additionally, CAT activity of the nanoenzyme (Fig. 1I) showed rapid oxygen dissolution in deoxygenated PBS (excess sodium sulfite), with higher oxygen dissolution observed in glucose-enriched conditions in DMSN-Cu@GOx/PEG, validating strong CAT activity.

Disulfide bonds are commonly used for designing glutathione (GSH)-responsive drug delivery systems, allowing controlled drug release upon GSH-triggered cleavage. The co-doping …S–S-S–S…bonds (originate from tetrasulfides precursor, BTES) in the mesoporous shell can induce intracellular GSH-mediated -S–S- redox reactions, accelerating biodegradation of silica nanoframework for drug release and disrupting redox homeostasis. Tumor cells exhibit significantly higher GSH levels than normal cells [22]. DMSN-Cu@GOx/PEG displays notable GSH responsiveness, with high intracellular GSH levels triggering release. We examined the impact of different GSH levels on Cu^{2+} release from DMSN-Cu@GOx/PEG, simulating extracellular (pH 7.4 + 2 μM GSH) and intracellular (pH 5 + 2 mM GSH) conditions. As shown in Fig. S4, copper ion leaching was negligible under the former condition but reached approximately 36% after 3 days under the latter condition, likely due to GSH-induced nanostructure degradation.

Synthesis and characterization of H@DMSN-Cu@GOx/PEG

The development of advanced integrated therapeutic solutions capable of rapidly hemostasis and loading anti-tumor drugs (hemostatic materials) is of paramount importance for advancing cancer treatment. Ca^{2+} significantly affects physiological coagulation pathways, activating Factor X. It participates in the formation of prothrombinase complex and activates Factor XIII to form insoluble fibrin polymers, exerting hemostatic effects [23, 24]. Following previously reported methods for synthesizing thermo-sensitive hydrogels [25], DMSN-Cu@GOx/PEG nanoenzyme was loaded onto these hydrogels with solubility as 5% (w/w), which possess high swelling capacity and distinct Ca^{2+} release characteristics, serving as hemostatic/anti-tumor dressings. As shown in Fig. S5A, scanning electron microscopy (SEM) characterized the surface morphology of the hydrogel, indicating a significant porous structure suitable for material loading. As shown in Fig. S5B, H@DMSN-Cu@GOx/PEG appeared as a transparent solution at 4 ℃, gradually transforming into a transparent hydrogel after being placed at 37 ℃ for a short period of time, exhibiting excellent thermo-sensitive properties that change physical characteristics near body temperature, suitable for post-surgical wound dressings in tumor operations.

In vitro anti-bladder cancer effects of DMSN-Cu@GOx/PEG

To investigate the in vitro anti-bladder cancer effects of DMSN-Cu@GOx/PEG, the proliferation viability of human bladder cancer cells (T24) was determined using the CCK-8 assay. As shown in Fig. S6, after 24 h of treatment, both DMSN-Cu@GOx/PEG and DMSN-Cu@PEG exhibited inhibitory effects on T24 cells in a dose-dependent manner, with DMSN-Cu@GOx/PEG demonstrating profoundly higher inhibition compared to DMSN-Cu@PEG. When the concentration of DMSN-Cu@GOx/PEG reached 40 μg/mL, the inhibition rate against T24 cells approached 50%, thus this concentration was chosen for subsequent experiments.

To further validate the inhibitory effect of DMSN-Cu@GOx/PEG on cell proliferation, flow cytometry was used to detect apoptosis in T24 cells. As shown in Fig. S7, both DMSN-Cu@GOx/PEG and DMSN-Cu@PEG induced apoptosis in T24 cells, with DMSN-Cu@GOx/PEG demonstrating a markedly higher induction of apoptosis

compared to DMSN-Cu@PEG. Additionally, Live/Dead staining analysis showed that in both DMSN-Cu@GOx/PEG and DMSN-Cu@PEG groups, substantial tumor cells exhibited red fluorescence, indicating cell death (Fig. S8). These results demonstrate that both DMSN-Cu@GOx/PEG and DMSN-Cu@PEG exhibit desirable efficacy in killing bladder cancer cells, with DMSN-Cu@GOx/PEG showing superior performance.

Construction of anoikis-resistance bladder cancer cell model (T24-AR)

The outcome of advanced bladder cancer often involves recurrence and distant metastasis, with distant metastasis being a major cause of death in bladder cancer patients [26]. Due to their invasive nature and resistance to apoptosis, surviving AR cells in circulation are considered crucial prerequisites for tumor metastasis and recurrence [27]. Therefore, understanding how to inhibit the AR capability of bladder cancer cells is a focus of our research. To simulate the metastatic pattern of bladder cancer cells in vivo, it is necessary to construct an AR bladder cancer cell model in vitro. We selected the human bladder cancer T24 cell line as the subject of our study for in vitro experiments and successfully constructed an AR bladder cancer cell model by culturing cells continuously in suspension for 1 week followed by reattachment to culture plates for 2 days. After successfully establishing the AR cell model, various experimental methods demonstrated that compared to parental cells, the malignant biological behaviors of AR cells were significantly enhanced, including apoptosis resistance and migration ability.

Cells that survived and proliferated after continuous suspension culture of T24 cells for 1 week on ultra-low attachment culture plates, followed by digestion and centrifugation, were identified as AR cells (Fig. S9). Using the CCK-8 assay to detect cell survival and proliferation at different suspension time points (1–7 days), the results showed that under continuous suspension conditions, the proliferation ability of the AR cell model (T24-AR) was significantly enhanced compared to the parental AR cell model (T24-P) (Fig. S10). Flow cytometry analysis of apoptosis levels showed that after 48 h of continuous suspension culture, the apoptosis rate of T24-AR cells was significantly lower than that of T24-P cells (Fig. S11). Similarly, Live/Dead staining analysis showed that the death rate of T24-AR cells was significantly lower than that of T24-P cells (Fig. S12). Additionally, we conducted Transwell experiments to evaluate the effect of AR on the migration ability of bladder cancer cells, and the results demonstrated that compared to parental cells, the migration ability of T24-AR cells was significantly enhanced (Fig. S13). In summary, after acquiring AR capability, bladder cancer cells exhibit significantly enhanced proliferation, anti-apoptosis, and migration abilities.

Induction of apoptosis in AR-bladder cancer cells by DMSN-Cu@GOx/PEG

The CCK-8 assay results showed that after 24 h of treatment, both DMSN-Cu@GOx/PEG and DMSN-Cu@PEG exhibited dose-dependent inhibition of T24 cells, with DMSN-Cu@GOx/PEG showing significantly higher inhibition than DMSN-Cu@PEG (Fig. 2A). The half-maximal inhibitory concentration (IC50) of DMSN-Cu@GOx/PEG against T24-AR cells was calculated to be 33.54 μM (Fig. 2B), and this concentration was used for subsequent experiments. Next, we investigated whether DMSN-Cu@GOx/PEG could induce apoptosis in AR-bladder cancer cells. Live/Dead staining and flow cytometry results demonstrated that DMSN-Cu@PEG induced apoptosis in some T24-AR cells, with DMSN-Cu@GOx/PEG showing most exceptional strong efficacy (Fig. 2C–E). Changes in the expression of apoptosis-related proteins directly reflect alterations in the AR of tumor cells [28]. Therefore, we examined the expression of apoptosis-related protein Bax and anti-apoptotic protein Bcl-2 in T24-AR cells. The results of Western blotting showed that DMSN-Cu@GOx/PEG prominently upregulated Bax expression and downregulated Bcl-2 expression in T24-AR cells (Fig. 2F–H), indicating that DMSN-Cu@GOx/PEG could notably weaken the AR capability of T24-AR cells.

Sustained high levels of oxidative stress can induce apoptosis in tumor cells through complex mechanisms, including induction of lipid peroxidation, protein oxidation damage, and DNA oxidation damage [29]. Intracellular ROS production in different groups was measured

(See figure on next page.)

Fig. 2 Anti-bladder cancer performance of nanoparticles in vitro. **A** Cell viability of T24-AR cells after treatment with different concentrations of DMSN@PEG, DMSN-Cu@PEG and DMSN-Cu@GOx/PEG (n = 3). **B** The IC50 of DMSN-Cu@GOx/PEG for anti-bladder cancer. **C** Fluorescence images of T24-AR cells co-stained with Calcein-AM (live cells, green) and PI (dead cells, red) upon different groups, Scale bar = 100 μm. **D** Flow cytometry (FCM) was used to detect the apoptosis of T24-AR cells (n = 3). **E** Corresponding apoptosis ratio of T24-AR cells after different treatments (n = 3). **F** Western blotting analysis of Bax and Bcl-2 expression in T24-AR cells (n = 3) and **G**, **H** the plot of the corresponding gray values (n = 3). **I**, **J** DCFH-DA probe was used to detect the level of ROS in T24-AR cells and corresponding DCFH-DA fluorescence intensity of T24-AR cells after different treatments (n = 3). **K** The quantitative analysis of the ratio of FL1/FL2 fluorescence intensity (n = 3). **L** JC-1 probe was used to measure the changes in mitochondrial membrane potential (MMP) in T24-AR cells (n = 3). *$P < 0.05$, **$P < 0.01$, ***$P < 0.001$

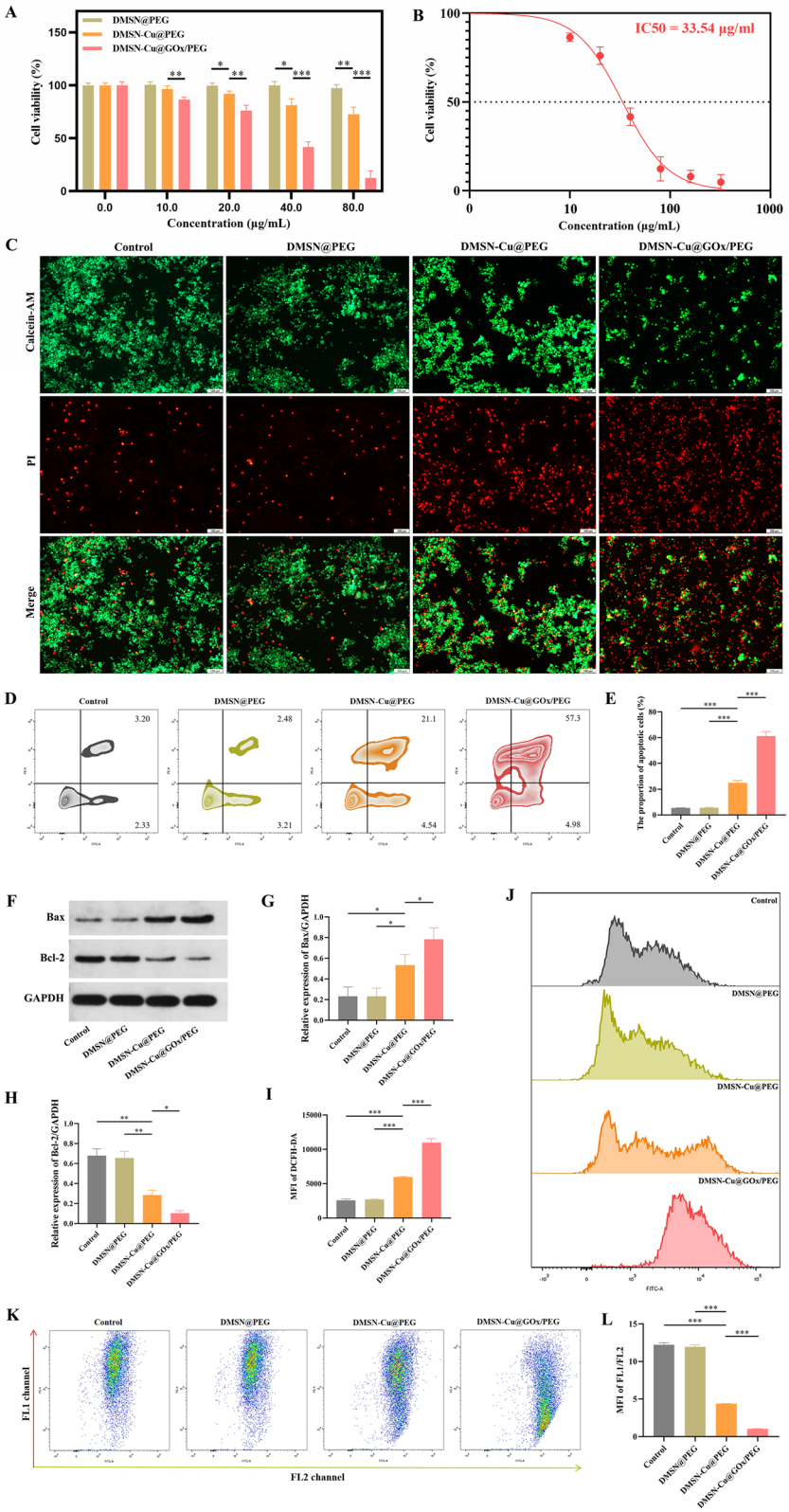

Fig. 2 (See legend on previous page.)

using DCFH-DA (a commercial ROS probe). As shown in Fig. 2I-J, both DMSN-Cu@PEG and DMSN-Cu@GOx/PEG treatments resulted in high ROS fluorescence intensity, with the DMSN-Cu@GOx/PEG group exhibiting significantly higher average fluorescence intensity than the DMSN-Cu@PEG group. Furthermore, mitochondria are the main sites of ROS production in cells, and under normal conditions, intracellular ROS can act as intracellular signaling molecules to regulate normal physiological functions of the body. When tissues are damaged, mitochondria produce large amounts of ROS, leading to mitochondrial dysfunction [30]. To investigate the dysfunction of mitochondria in the apoptosis process induced by DMSN-Cu@GOx/PEG in T24-AR cells, we measured changes in mitochondrial membrane potential (MMP) using the JC-1 probe. Under normal circumstances, the JC-1 probe accumulates in mitochondria in an aggregated form. When mitochondria are damaged and MMP decreases, the JC-1 probe is released into the cytoplasm in a monomeric form [31]. As shown in Fig. 2K-L, treatment with DMSN-Cu@GOx/PEG dramatically decreased MMP in T24-AR cells. These results confirmed that both DMSN-Cu@GOx/PEG and DMSN-Cu@PEG can damage mitochondria in AR-bladder cancer cells, promote excessive ROS production within cells, and thereby weaken AR capability of bladder cancer cells.

DMSN-Cu@GOx/PEG suppresses EMT process in AR-bladder cancer cells

Yu et al. [27] and our results (Fig. S13) have both confirmed that AR-tumor cells exhibit much higher migratory ability than parental cells. Therefore, we investigate whether DMSN-Cu@GOx/PEG can reduce the migratory ability of AR-bladder cancer cells, thereby achieving the purpose of inhibiting the metastasis and recurrence of bladder cancer. As shown in Fig. 3A, B, the results of Transwell assay confirmed that both DMSN-Cu@GOx/PEG and DMSN-Cu@PEG can reduce the number of transmembrane migrations of T24-AR cells, inhibiting their migratory ability, with DMSN-Cu@GOx/PEG showing particularly significant effects. EMT is one of the important mechanisms underlying tumor metastasis. The occurrence of EMT promotes epithelial cell polarization, endowing them with mesenchymal characteristics, thereby enhancing cell migration and invasion abilities. Therefore, activation of EMT is considered a key step in initiating tumor metastasis [32]. During EMT process, epithelial polarity and cell connections are lost. E-cadherin maintains tight intercellular connections, preventing cell invasion and metastasis. Loss of E-cadherin expression is recognized as the most significant feature of EMT [33]. N-cadherin is a major component of intercellular adhesion, mediating dynamic adhesion between tumor cells and increasing cell motility and invasiveness [33]. Vimentin, a type of intermediate filament protein, is also one of the main markers of EMT and is closely related to tumor occurrence and metastasis [33, 34]. As shown in Fig. 3C, E–G, DMSN-Cu@GOx/PEG substantially upregulated E-cadherin expression in T24-AR cells and concurrently downregulated N-cadherin and Vimentin expression. These results indicated that DMSN-Cu@GOx/PEG can inhibit the EMT process in AR-bladder cancer cells, thereby reducing their migratory ability.

Inspired by above findings, we investigated the specific mechanism by which DMSN-Cu@GOx/PEG inhibits EMT in T24-AR cells. Hypoxia is one of the most common features of TME, driving tumor invasiveness [35]. Overexpression of HIF-1α is closely associated with tumor metastasis and increased mortality. Hypoxia-inducible factor-1 (HIF-1) activates the transcription of hundreds of downstream genes involved in various aspects of cancer development under low oxygen conditions, triggering adaptive cellular responses [36, 37]. HIF-1 is a heterodimeric transcription factor composed of α and β subunits [37]. Oxygen level changes do not affect HIF-1α expression, but its expression level is strictly regulated by intracellular oxygen concentration [37, 38]. The α subunit primarily controls HIF-1 activity, regulating its stability and transcriptional activity in multiple aspects. Tumor cells in a state of EMT often exhibit low ROS levels and upregulated HIF-1 activity [39]. Silencing HIF-1α significantly weakens tumor cell resistance, indicating the important role of HIF-1α in the process of tumor cell resistance acquisition [39]. Previous study have suggested that silencing HIF-1α makes tumor cells sensitive to anchorage dependence, impairs sphere formation, increases integrin α5 expression, and induces anoikis of tumor cells [40]. In summary, due to the presence of a hypoxic TME, high levels of intracellular HIF-1 play an important role in promoting cancer development and acquiring AR capability [41]. Therefore, targeting the regulation of oxygen levels in tumors to regulate HIF-1 expression may be an important therapeutic approach to inhibit tumor proliferation and increase anoikis sensitivity. As shown in Fig. 3D and H, in sharp contrast to other groups, DMSN-Cu@GOx/PEG significantly downregulated HIF-1α protein expression in T24-AR cells. This may be attributed to DMSN-Cu@GOx/PEG effectively converting high levels of H_2O_2 generated by intracellular GOx catalysis into O_2, thereby alleviating tumor hypoxia and attenuating HIF-1α expression. Interestingly, EMT is regulated by many transcription factors, with HIF-1α being one of the most important transcription factors [42]. Intracellular HIF-1α in tumor

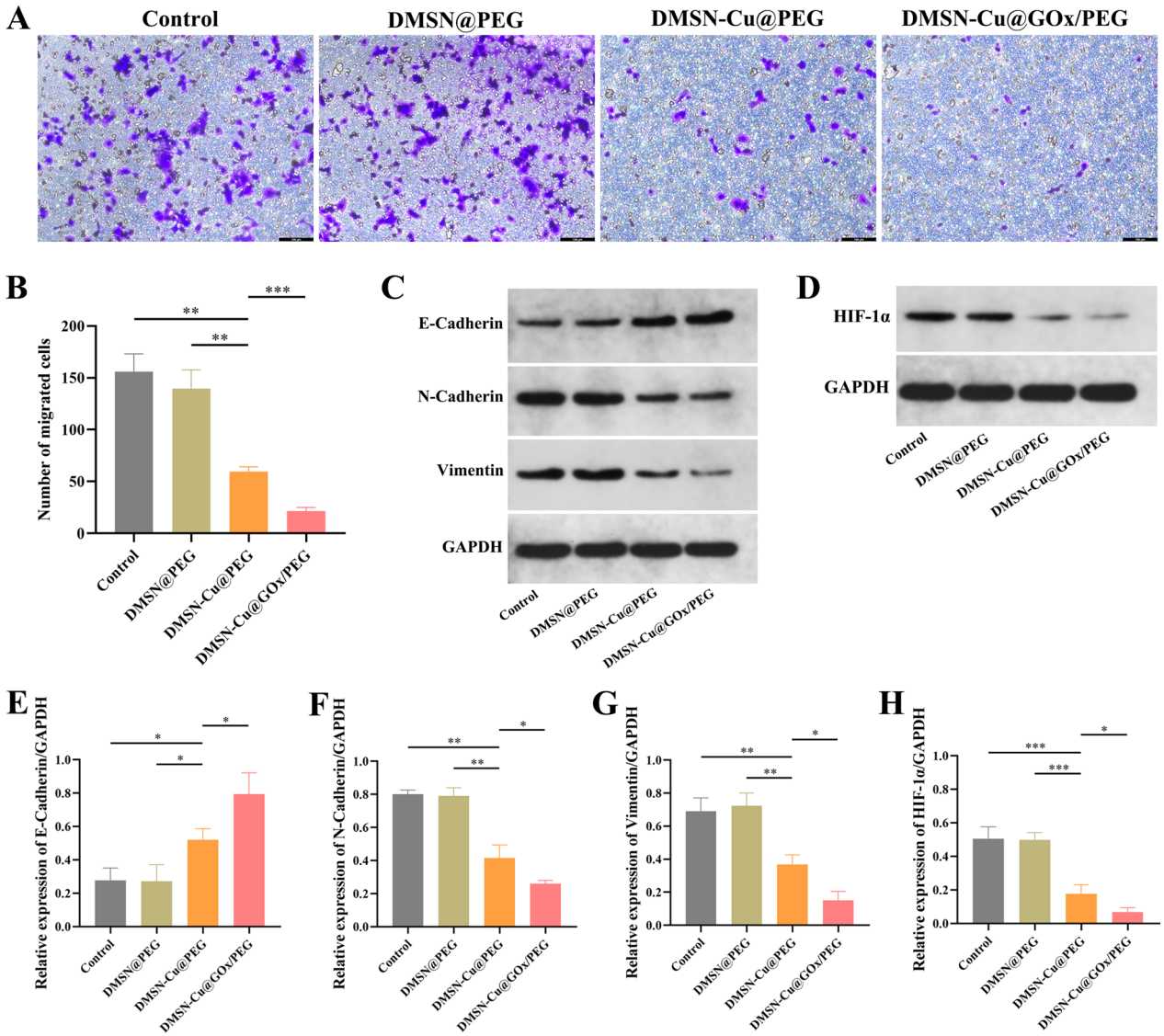

Fig. 3 Nanoparticles inhibit the migration and epithelial-mesenchymal transition (EMT) progression of bladder cancer cells in vitro. **A** Representative images of Transwell assay of T24-AR cells (n = 3). Scale bar = 100 μm. **B** Number of migrated cells of T24-AR cells (n = 3). **C** Western blotting analysis of E-Cadherin, N-Cadherin and Vimentin expression in T24-AR cells (n = 3) and (**E**, **F**) the plot of the corresponding gray values. **D** Western blotting analysis of HIF-1α expression in T24-AR cells (n = 3) and (**G**, **H**) the plot of the corresponding gray values (n = 3). *$P < 0.05$, **$P < 0.01$, ***$P < 0.001$

cells cooperates with the expression of EMT-related transcription factors, directly or indirectly regulating and inducing the expression of EMT-related genes, as well as modulating the interactions between various factors, thereby promoting EMT process [43]. Accordingly, the inhibition of HIF-1α significantly upregulates E-cadherin expression, downregulates N-cadherin and Vimentin expression, and blocks the EMT process [44, 45]. Collectively, DMSN-Cu@GOx/PEG can effectively downregulate HIF-1α expression in AR-bladder cancer cells, blocking their EMT process and reducing their migratory ability.

H@DMSN-Cu@GOx/PEG exhibited excellent hemostatic performance

Tumor tissues are characterized by a dense local blood supply and harbor numerous abnormal neovascularizations. Consequently, bleeding during tumor resection is unavoidable and presents huge challenges during surgical intervention. Furthermore, substantial intraoperative bleeding adversely impacts prognosis [24, 46].

Intraoperative bleeding undoubtedly increases the risk of tumor recurrence due to cancer cell dissemination [47]. Although some commercial hemostatic materials such as QuickClot®, glutaraldehyde cross-linked albumin, and fibrin bandages are used to treat superficial bleeding conditions, simple gauze packing is mainly used in malignant tumor surgeries [24, 48, 49]. However, the hemostatic performance of gauze is limited and lacks anti-tumor recurrence and metastasis functions. Proper selection and application of high-performance hemostatic and anti-cancer materials can effectively reduce intraoperative bleeding, assist in clearing the surgical field, and reduce surgical difficulty. These materials can also reduce postoperative recurrence and improve prognosis. Therefore, the development of effective hemostatic and anti-cancer materials with clinical application value is crucial.

The synthesized H@DMSN-Cu@GOx/PEG thermosensitive hydrogel, characterized by high swelling properties and distinct Ca^{2+} release characteristics, represents a promising candidate for hemostatic materials in postoperative tumor scenarios owing to its exceptional chemical-biological attributes. We assessed the emergency hemostatic performance of H@DMSN-Cu@GOx/PEG using a mouse liver hemostasis model for acute bleeding events [50]. Without hemostatic material treatment, liver bleeding lasted 128.3 ± 14.3 s. The standard medical gauze treatment group and the hydrogel precursor (without Ca^{2+}) treatment group exhibited bleeding times of 63.7 ± 11.5 s and 73.7 ± 7.1 s, respectively, while the H@DMSN-Cu@GOx/PEG treatment group had a bleeding time of 57 ± 7 s (Fig. 4A, B). This underscores the excellent visceral organ hemostatic ability of H@DMSN-Cu@GOx/PEG, attributed to its thermosensitivity, rapid expansion properties, and Ca^{2+} release capacity. Upon contact with the wound, H@DMSN-Cu@GOx/PEG rapidly expands, exerting physical pressure to effectively arrest further bleeding. Moreover, H@DMSN-Cu@GOx/PEG elevates local Ca^{2+} concentration, a critical factor affecting the physiological coagulation pathway by activating Factor X, contributing to prothrombinase complex formation, and activating Factor XIII to produce insoluble fibrin polymers, thus exerting hemostatic effects [23, 24]. Additionally, we evaluated the hemostatic effect of H@DMSN-Cu@GOx/PEG by measuring liver bleeding. As depicted in Fig. 4C, D, H@DMSN-Cu@GOx/PEG treatment resulted in the lowest relative OD value in abdominal lavage fluid post-liver wound hemostasis, indicative of reduced liver bleeding and enhanced clotting ability within the H@DMSN-Cu@GOx/PEG group. Subsequently, we assessed H@DMSN-Cu@GOx/PEG's hemostatic ability through an in vitro coagulation test. As demonstrated in Fig. 4E, F, both the hydrogel precursor and H@DMSN-Cu@GOx/PEG exhibited significantly lower blood clotting indices compared to the control group, with H@DMSN-Cu@GOx/PEG demonstrating excellent in vitro coagulation performance.

H@DMSN-Cu@GOx/PEG exhibited excellent biocompatibility

In order to appraise the cellular toxicity of the hydrogel formulations and to substantiate the biological safety of H@DMSN-Cu@GOx/PEG, co-culture experiments were conducted involving mouse fibroblast L929 cells. These cells were exposed to PBS, H@DMSN@PEG, H@DMSN-Cu@PEG, and H@DMSN-Cu@GOx/PEG separately. The assessment of cell viability and proliferative ability was carried out utilizing Live/Dead staining in conjunction with CCK-8 assay. As depicted in Fig. 5A, B, treatment of L929 cells with 10 μL of H@DMSN@PEG, H@DMSN-Cu@PEG or H@DMSN-Cu@GOx/PEG did not affect cell viability, with cell survival rates nearly reaching 100%. Additionally, hemolysis tests were conducted to evaluate the blood compatibility of the microspheres. As shown in Fig. 5C, the hemolysis rates of H@DMSN@PEG, H@DMSN-Cu@PEG and H@DMSN-Cu@GOx/PEG groups were less than 5%, indicating excellent blood compatibility.

To assess the in vivo toxicity of the hydrogel, 10 μL of H@DMSN@PEG, H@DMSN-Cu@PEG or H@DMSN-Cu@GOx/PEG was injected into the abdominal cavities of mice. After 7 days, heart, liver, spleen, lung, and kidney tissues were collected and stained with hematoxylin and eosin (H&E). Histological examination revealed no signs of inflammation or lesions (Fig. 5D). In summary, H@DMSN@PEG, H@DMSN-Cu@PEG and H@DMSN-Cu@GOx/PEG exhibited no significant biotoxicity in vitro and in vivo, confirming their excellent biocompatibility.

H@DMSN-Cu@GOx/PEG suppresses postoperative tumor recurrence in vivo

To rigorously assess the therapeutic efficacy of H@DMSN@PEG, H@DMSN-Cu@PEG, and H@DMSN-Cu@GOx/PEG in mitigating postoperative tumor recurrence, a comprehensive in vivo tumor model was meticulously established. Specifically, T24 bladder cancer cells were subcutaneously inoculated into the right hind flank region of immunodeficient Balb/c-nude mice, simulating the presence of a solid tumor mass. Once the tumors achieved a volume of approximately 100 mm^3, indicative of a clinically relevant tumor burden, 25 mice were meticulously randomized into five distinct experimental cohorts to ensure statistical power and validity (Fig. 6A).

The first cohort served as a negative control, receiving no therapeutic intervention post-tumor establishment. The second group underwent surgical excision of the

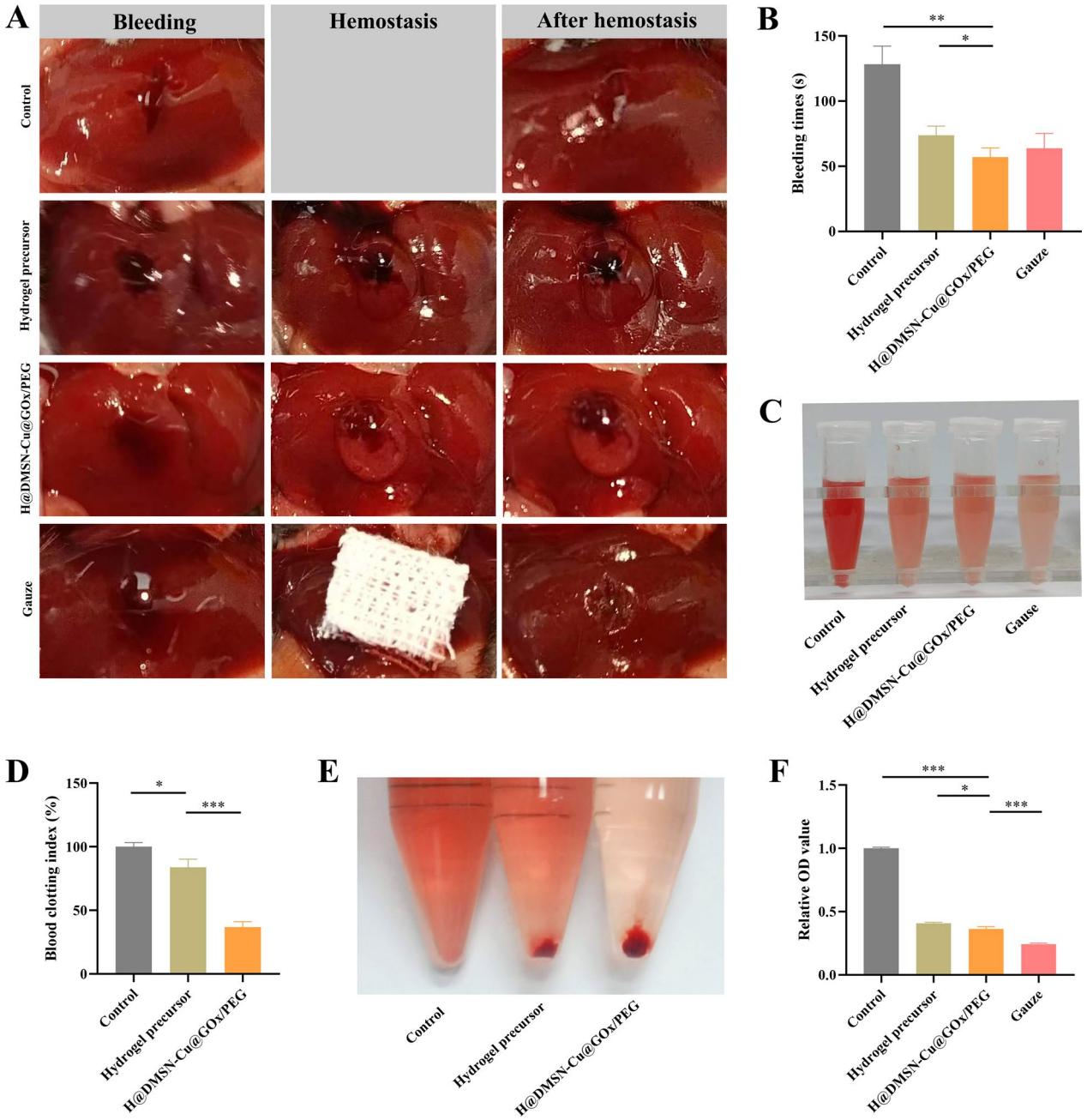

Fig. 4 H@DMSN-Cu@GOx/PEG exhibited excellent hemostatic performance. **A** Photographs for the bleeding wound with untreated, treated and removed hydrogel precursor, H@DMSN-Cu@GOx/PEG and gauze, respectively, in mouse liver hemostasis model (n = 3). **B** Bleeding time of wounds in different groups (n = 3). **C** Abdominal cavity lavage fluid photograph and (**D**) the corresponding relative OD values after NEMs treatment (n = 3). **E** Photographs from the in vitro blood-clotting measurement and **F** the corresponding relative OD values of the supernatant absorbance (n = 3). $^{*}P < 0.05$, $^{**}P < 0.01$, $^{***}P < 0.001$

tumor, representing a conventional treatment scenario without adjuvant therapy. The third cohort received surgical resection followed by the topical administration of H@DMSN@PEG, aiming to evaluate the impact of a standard hydrogel formulation on postoperative tumor behavior. The fourth group was subjected to tumor resection and subsequently treated with H@DMSN-Cu@PEG, hypothesizing that the inclusion of copper ions could confer additional therapeutic benefits. Lastly, the fifth group underwent tumor excision and was administered H@DMSN-Cu@GOx/PEG, integrating the advantages of copper ions with the enzymatic activity of GOx

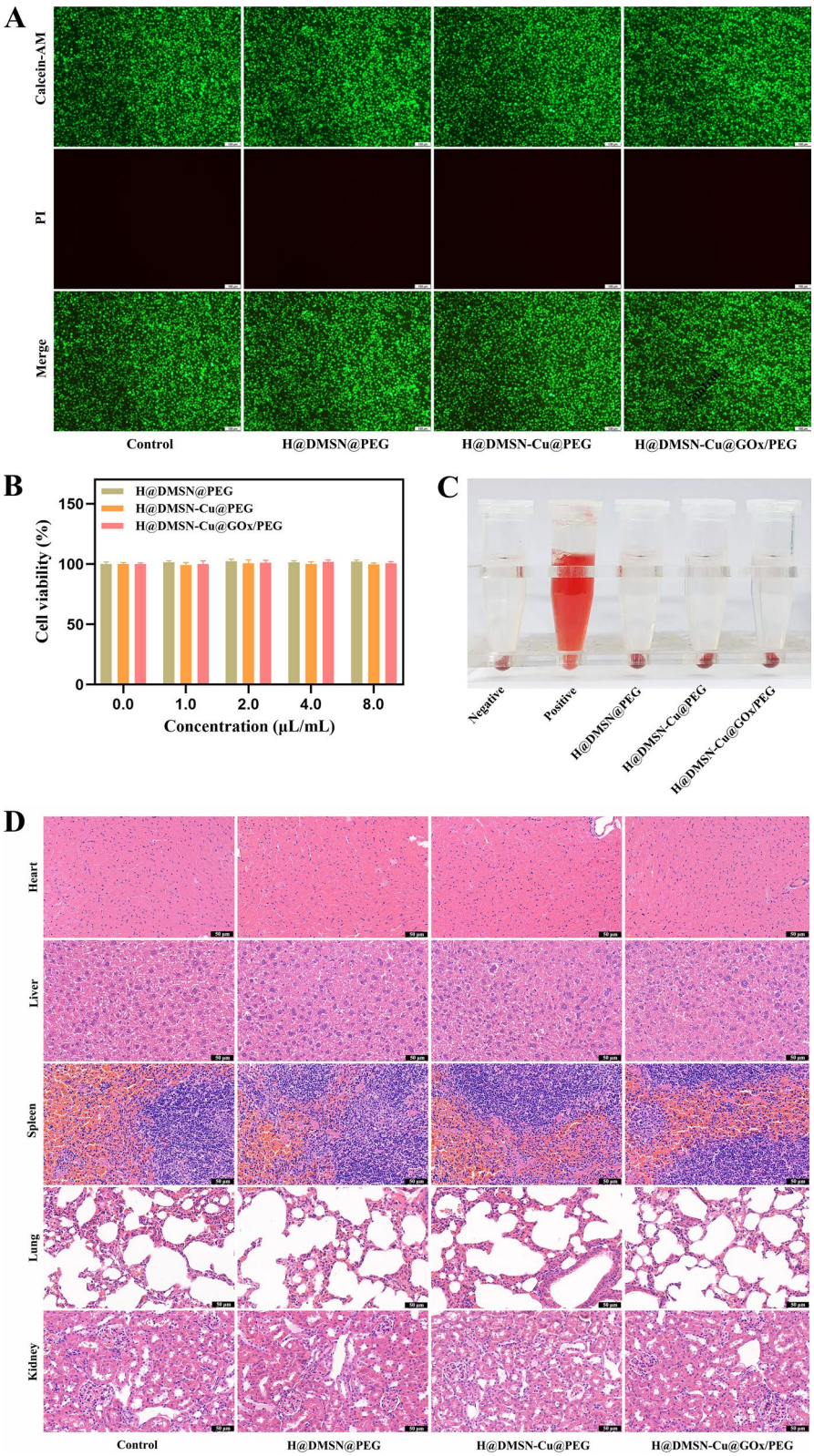

Fig. 5 H@DMSN-Cu@GOx/PEG exhibited excellent biocompatibility. **A** Fluorescence images of L929 cells co-stained with Calcein-AM and PI upon different groups, Scale bar = 100 μm. **B** Cell viability of L929 cells after treatment with different concentrations in different groups (n = 3). **C** Blood compatibility in different groups (n = 3). **D** Histological examination of hearts, livers, spleens, lungs and kidneys (n = 3), Scale bar = 50 μm. *$P < 0.05$, **$P < 0.01$, ***$P < 0.001$

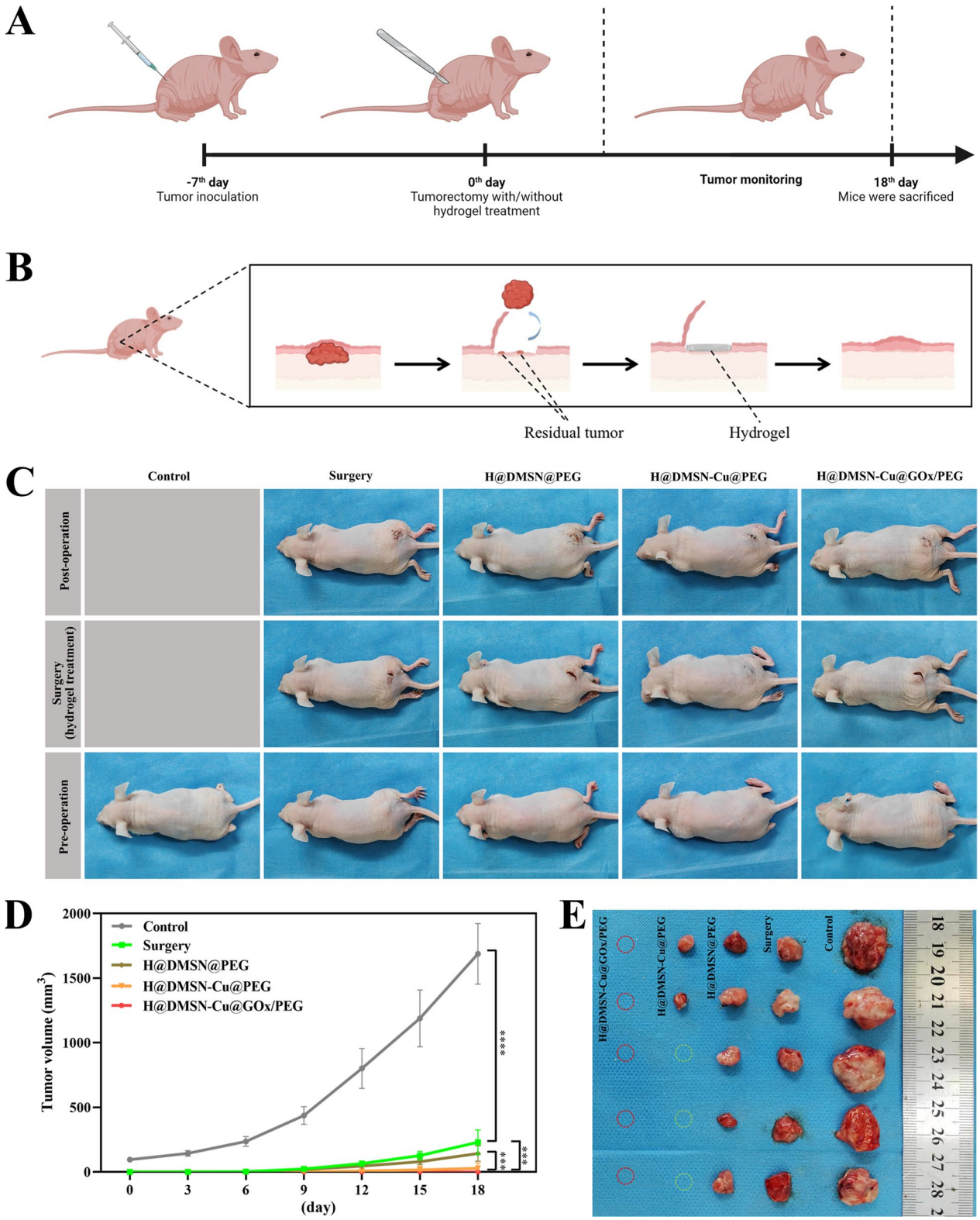

Fig. 6 H@DMSN-Cu@GOx/PEG suppresses postoperative tumor recurrence in vivo. **A** Schematic representation of the hydrogel therapy for tumor-bearing mice. **B** Schematic representation of the surgical treatment and post-surgical treatment of the tumor. **C** Typical photographs of the tumor-bearing mice without any treatment, surgical treatment only, H@DMSN@PEG treatment, H@DMSN-Cu@PEG treatment, and H@DMSN-Cu@GOx/PEG treatment (n = 5). **D** Corresponding tumors growth curves of the tumor-bearing mice (n = 5). **E** Digital photographs of tumors in each group (n = 5). ***$P < 0.001$, ****$P < 0.0001$

to test the hypothesis that this combination could offer superior anti-tumor efficacy.

Post-surgical procedures, the tumor site was meticulously prepared by creating a precise incision at the tumor's perimeter, followed by the complete excision of the neoplasm. Subsequently, the respective hydrogel formulations were applied to the surgical wound, forming a protective and therapeutic barrier (Fig. 6B). Throughout the experimental duration, tumor volumes were diligently quantified at regular intervals of 3 days to monitor tumor dynamics and response to treatment.

Throughout the treatment regimen, the health status of the mice was continuously monitored for any signs of adverse effects. Importantly, no untoward incidents such as mortality or significant deviations in body weight or dietary habits were noted, suggesting the overall safety profile of the hydrogel formulations. As illustrated in Figs. 6C–E, the cohort subjected solely to tumor resection experienced a pronounced resurgence of tumor growth, underscoring the limitations of surgical intervention alone in preventing tumor recurrence. Notably, within the H@DMSN-Cu@PEG-treated cohort, a significant subset of mice exhibited an absence of tumor recurrence. More strikingly, all mice within the H@DMSN-Cu@GOx/PEG group displayed an exceptional resistance to neoplastic regrowth post-surgery, potentially due to the synergistic effects of copper ions and GOx in the context of ECDT. Collectively, these observations provide compelling evidence for the effectiveness of the hydrogel we developed in preventing tumor recurrence following surgical intervention, highlighting their potential clinical utility in oncology for managing postoperative tumor recurrence. These findings collectively underscore the potential of H@DMSN-Cu@PEG and H@DMSN-Cu@GOx/PEG to effectively suppress tumor recurrence post-resection to varying degrees, with H@DMSN-Cu@GOx/PEG exhibiting a particularly strong anti-recurrence profile. This research not only advances our understanding of the mechanisms underlying tumor recurrence but also paves the way for the development of novel therapeutic strategies to improve postoperative outcomes in bladder cancer patients.

Conclusion

In summary, an anion-assisted methodology was employed to engineer a dendritic mesoporous silica-based nanocomposite encapsulated with Cu^{2+} (DMSN-Cu@GOx/PEG), further enfolded within a thermosensitive hydrogel (H@DMSN-Cu@GOx/PEG). This innovative nanoconstruct and hydrogel formulation are designed to counteract the AR capabilities of tumor cells, prevent intraoperative hemorrhage, and mitigate postoperative tumor recurrence. Our investigation represents a pioneering effort in employing dendrimeric mesoporous silica-based nanoreactors to suppress the AR of bladder cancer cells and to curb the recurrence of tumors following surgical intervention, thus charting a novel course in the strategic prevention of postoperative tumor recurrence.

However, the present study is not without its limitations. Although H@DMSN-Cu@GOx/PEG demonstrated favorable antineoplastic efficacy in animal models, their safety and efficacy in human subjects remain to be substantiated. A translational gap exists between preclinical studies and human applications, necessitating clinical trials to corroborate these findings. Furthermore, our study might lack comprehensive long-term follow-up data post-treatment, encompassing both the effectiveness of the therapy and potential adverse effects or complications. Longitudinal safety evaluations are indispensable to ascertain the viability of any therapeutic modality. Moreover, bladder cancer exhibits considerable heterogeneity, and different patients may exhibit variable responses to identical treatment regimens. A larger sample size and a broader patient cohort would be essential to assess the consistency and generalizability of the treatment outcomes. Collectively, while acknowledging the limitations of the current study, we anticipate that these shortcomings will be systematically addressed and rectified in future endeavors.

Supplementary Information

The online version contains supplementary material available at https://doi.org/10.1186/s12951-024-02739-3.

Additional file 1.

Acknowledgements
Yang Liu and Lei Ding contributed equally to this work.

Author contributions
Y.L.: Funding acquisition, Investigation, Resources, Software, Writing—original draft. L.D.: Investigation, Software, Writing—original draft, Writing—review &editing. G.C.: Resources, Software, Investigation. P.W.: Funding acquisition, Investigation, Supervision, Writing—review & editing. X.W.: Funding acquisition, Investigation, Supervision, Writing—review & editing.

Funding
This work was supported by the Program of Excellent Doctoral of Zhongnan Hospital of Wuhan University (No. ZNYB2021018) and the Fundamental Research Funds for the Central Universities (No. 2042022dx0003), Natural Science Foundation of Fujian Province (No. 2021J05286) and Natural Science Foundation of Xiamen City (No. 3502Z202373073).

Data availability
No datasets were generated or analysed during the current study.

Declarations

Competing interests
The authors declare no competing interests.

Author details
[1]Department of Urology, Zhongnan Hospital of Wuhan University, Wuhan 430071, People's Republic of China. [2]Hubei Key Laboratory of Urological Diseases, Wuhan University, Wuhan 430071, People's Republic of China. [3]School of Rare Earths, University of Science and Technology of China, Hefei 230026, People's Republic of China. [4]Ganjiang Innovation Academy, Chinese Academy of Sciences, Ganzhou 341000, People's Republic of China. [5]Key Laboratory of Design and Assembly of Functional Nanostructures, Fujian Institute of Research On the Structure of Matter, Chinese Academy of Sciences, Fuzhou 350002, People's Republic of China. [6]Medical Research Institute, Wuhan University, Wuhan 430071, People's Republic of China. [7]Taikang Center for Life and Medical Sciences, Wuhan University, Wuhan 430071, People's Republic of China.

Received: 4 June 2024 Accepted: 24 July 2024
Published online: 20 August 2024

References

1. Bray F, Ferlay J, Soerjomataram I, Siegel RL, Torre LA, Jemal A. Global cancer statistics 2018: GLOBOCAN estimates of incidence and mortality worldwide for 36 cancers in 185 countries. CA-Cancer J Clin. 2018;68(6):394–424.
2. Siegel RL, Miller KD, Jemal A. Cancer statistics, 2018. CA-Cancer J Clin. 2018;68(1):7–30.
3. Mun DH, Kimura S, Shariat SF, Abufaraj M. The impact of gender on oncologic outcomes of bladder cancer. Curr Opom Urol. 2019;29(3):279–85.
4. Divrik RT, Sahin AF, Yildirim U, Altok M, Zorlu F. Impact of routine second transurethral resection on the long-term outcome of patients with newly diagnosed pT1 urothelial carcinoma with respect to recurrence, progression rate, and disease-specific survival: a prospective randomised clinical trial. Eur Urol. 2010;58(2):185–90.
5. Merkow RP, Bilimoria KY, Tomlinson JS, Paruch JL, Fleming JB, Talamonti MS, Ko CY, Bentrem DJ. Postoperative complications reduce adjuvant chemotherapy use in resectable pancreatic cancer. Ann Surg. 2014;260(2):372–7.
6. Simpson CD, Anyiwe K, Schimmer AD. Anoikis resistance and tumor metastasis. Cancer Lett. 2008;272(2):177–85.
7. Dai Y, Zhang X, Ou Y, Zou L, Zhang D, Yang Q, Qin Y, Du X, Li W, Yuan Z, et al. Anoikis resistance –protagonists of breast cancer cells survive and metastasize after ECM detachment. Cell Commun Signal. 2023. https://doi.org/10.1186/s12964-023-01183-4.
8. Liotta LA, Kohn E. Anoikis—cancer and the homeless cell. Nature. 2004;430(7003):973–4.
9. Wang Y, Zeng Z, Lu J, Wang Y, Liu Z, He M, Zhao Q, Wang Z, Li T, Lu Y, et al. CPT1A-mediated fatty acid oxidation promotes colorectal cancer cell metastasis by inhibiting anoikis. Oncogene. 2018;37(46):6025–40.
10. Lequeux A, Noman MZ, Xiao M, Van Moer K, Hasmim M, Benoit A, Bosseler M, Viry E, Arakelian T, Berchem G, et al. Targeting HIF-1 alpha transcriptional activity drives cytotoxic immune effector cells into melanoma and improves combination immunotherapy. Oncogene. 2021;40(28):4725–35.
11. Kadkhoda J, Tarighatnia A, Nader ND, Aghanejad A. Targeting mitochondria in cancer therapy: insight into photodynamic and photothermal therapies. Life Sci. 2022;307:120898.
12. Siminzar P, Tohidkia MR, Eppard E, Vahidfar N, Tarighatnia A, Aghanejad A. Recent trends in diagnostic biomarkers of tumor microenvironment. Mol Imaging Biol. 2023;25(3):464–82.
13. Li X, Wang M, Li S, Chen Y, Wang M, Wu Z, Sun X, Yao L, Dong H, Song Y, et al. HIF-1-induced mitochondrial ribosome protein L52: a mechanism for breast cancer cellular adaptation and metastatic initiation in response to hypoxia. Theranostics. 2021;11(15):7337–59.
14. Ang HL, Mohan CD, Shanmugam MK, Leong HC, Makvandi P, Rangappa KS, Bishyaee A, Kumar AP, Sethi G. Mechanism of epithelial-mesenchymal transition in cancer and its regulation by natural compounds. Med Res Rev. 2023;43(4):1141–200.
15. Akrida I, Papadaki H. Adipokines and epithelial-mesenchymal transition (EMT) in cancer. Mol Cell Biochem. 2023;478(11):2419–33.
16. Nepali PR, Kyprianou N. Anoikis in phenotypic reprogramming of the prostate tumor microenvironment. Front Endocrinol. 2023. https://doi.org/10.3389/fendo.2023.1160267.
17. Fonseca I, Horta C, Ribeiro AS, Sousa B, Marteil G, Bettencourt-Dias M, Paredes J. Polo-like kinase 4 (Plk4) potentiates anoikis -resistance of p53KO mammary epithelial cells by inducing a hybrid EMT phenotype. Cell Death Dis. 2023. https://doi.org/10.1038/s41419-023-05618-1.
18. Liu Z, Tang W, Liu J, Han Y, Yan Q, Dong Y, Liu X, Yang D, Ma G, Cao H. A novel sprayable thermosensitive hydrogel coupled with zinc modified metformin promotes the healing of skin wound. Bioact Mater. 2023;20:610–26.
19. Xiong Y, Wang T, Liu L, Kou Y, Zhao Z, Yuan M, Chen Y, Wang D, Song S. Hydrogelation of TPGS for locoregional combination therapy of cancer. Chem Eng J. 2023;451:138889.
20. Zhang K, Xue K, Loh XJ. Thermo-responsive hydrogels: from recent progress to biomedical applications. Gels. 2021;7(3):77.
21. Weng H, Jia W, Li M, Chen Z. New injectable chitosan-hyaluronic acid based hydrogels for hemostasis and wound healing. Carbohyd Polym. 2022;294:119767.
22. Bansal A, Simon MC. Glutathione metabolism in cancer progression and treatment resistance. J Cell Biol. 2018;217(7):2291–8.
23. Subramaniam T, Fauzi MB, Lokanathan Y, Law JX. The role of calcium in wound healing. Int J Mol Sci. 2021;22(12):6486.
24. Guo Y, Wang M, Liu Q, Liu G, Wang S, Li J. Recent advances in the medical applications of hemostatic materials. Theranostics. 2023;13(1):161–96.
25. Wang C, Wang M, Xu T, Zhang X, Lin C, Gao W, Xu H, Lei B, Mao C. Engineering bioactive self-healing antibacterial exosomes hydrogel for promoting chronic diabetic wound healing and complete skin regeneration. Theranostics. 2019;9(1):65–76.
26. Song Q, Yu H, Cheng Y, Han J, Li K, Zhuang J, Lv Q, Yang X, Yang H. Bladder cancer-derived exosomal KRT6B promotes invasion and metastasis by inducing EMT and regulating the immune microenvironment. J Transl Med. 2022;20(1):308.
27. Yu Y, Song Y, Cheng L, Chen L, Liu B, Lu D, Li X, Li Y, Lv F, Xing Y. CircCEMIP promotes anoikis-resistance by enhancing protective autophagy in prostate cancer cells. J Exp Clin Canc Res. 2022;41(1):188.
28. Huang W, Liu C, Liu F, Liu Z, Lai G, Yi J. Hinokiflavone induces apoptosis and inhibits migration of breast cancer cells via EMT signalling pathway. Cell Biochem Funct. 2020;38(3):249–56.
29. Zhao Y, Ye X, Xiong Z, Ihsan A, Ares I, Martinez M, Lopez-Torres B, Martinez-Larranaga MR, Anadon A, Wang X, et al. Cancer metabolism: the role of ROS in DNA damage and induction of apoptosis in cancer cells. Metabolites. 2023;13(7):796.
30. Li A, Lian L, Chen X, Cai W, Fan X, Fan Y, Li T, Xie Y, Zhang J. The role of mitochondria in myocardial damage caused by energy metabolism disorders: from mechanisms to therapeutics. Free Radical Bio Med. 2023;208:236–51.
31. Chen L, Chen G, Hu K, Chen L, Zeng Z, Li B, Jiang G, Liu Y. Combined photothermal and photodynamic therapy enhances ferroptosis to prevent cancer recurrence after surgery using nanoparticle-hydrogel composite. Chem Eng J. 2023;468:143685.
32. Krebs AM, Mitschke J, Lasierra LM, Schmalhofer O, Boerries M, Busch H, Boettcher M, Mougiakakos D, Reichardt W, Bronsert P, et al. The EMT-activator Zeb1 is a key factor for cell plasticity and promotes metastasis in pancreatic cancer. Nat Cell Biol. 2017;19(5):518–29.
33. Fontana R, Mestre-Farrera A, Yang J. Update on epithelial-mesenchymal plasticity in cancer progression. Annu Rev Pathol-Mech. 2023. https://doi.org/10.1146/annurev-pathmechdis-051222-122423.
34. Xuan B, Ghosh D, Dawson MR. Contributions of the distinct biophysical phenotype of polyploidal giant cancer cells to cancer progression. Semin Cancer Biol. 2022;81:64–72.
35. Hielscher A, Gerecht S. Hypoxia and free radicals: role in tumor progression and the use of engineering-based platforms to address these relationships. Free Radical Bio Med. 2015;79:281–91.
36. Meijer TW, Kaanders JH, Span PN, Bussink J. Targeting hypoxia, HIF-1, and tumor glucose metabolism to improve radiotherapy efficacy. Clin Cancer Res. 2012;18(20):5585–94.
37. Kheshtchin N, Hadjati J. Targeting hypoxia and hypoxia-inducible factor-1 in the tumor microenvironment for optimal cancer immunotherapy. J Cell Physiol. 2022;237(2):1285–98.

38. Kaelin WJ, Ratcliffe PJ. Oxygen sensing by metazoans: the central role of the HIF hydroxylase pathway. Mol Cell. 2008;30(4):393–402.
39. Maurer GD, Brucker DP, Steinbach JP. Loss of cell-matrix contact increases hypoxia-inducible factor-dependent transcriptional activity in glioma cells. Biochem Bioph Res Co. 2019;515(1):77–84.
40. Rohwer N, Welzel M, Daskalow K, Pfander D, Wiedenmann B, Detjen K, Cramer T. Hypoxia-inducible factor 1alpha mediates anoikis resistance via suppression of alpha5 integrin. Cancer Res. 2008;68(24):10113–20.
41. Adeshakin FO, Adeshakin AO, Afolabi LO, Yan D, Zhang G, Wan X. Mechanisms for modulating anoikis resistance in cancer and the relevance of metabolic reprogramming. Front Oncol. 2021;11:626577.
42. Zhang L, Huang G, Li X, Zhang Y, Jiang Y, Shen J, Liu J, Wang Q, Zhu J, Feng X, et al. Hypoxia induces epithelial-mesenchymal transition via activation of SNAI1 by hypoxia-inducible factor -1alpha in hepatocellular carcinoma. BMC Cancer. 2013;13:108.
43. Mirzaei S, Ranjbar B, Tackallou SH, Aref AR. Hypoxia inducible factor-1alpha (HIF-1alpha) in breast cancer: the crosstalk with oncogenic and onco-suppressor factors in regulation of cancer hallmarks. Pathol Res Pract. 2023;248:154676.
44. Gao XZ, Wang GN, Zhao WG, Han J, Diao CY, Wang XH, Li SL, Li WC. Blocking OLFM4/HIF-1alpha axis alleviates hypoxia-induced invasion, epithelial-mesenchymal transition, and chemotherapy resistance in non-small-cell lung cancer. J Cell Physiol. 2019;234(9):15035–43.
45. Bian Y, Yin G, Wang G, Liu T, Liang L, Yang X, Zhang W, Tang D. Degradation of HIF-1alpha induced by curcumol blocks glutaminolysis and inhibits epithelial-mesenchymal transition and invasion in colorectal cancer cells. Cell Biol Toxicol. 2023;39(5):1957–78.
46. Viallard C, Larrivee B. Tumor angiogenesis and vascular normalization: alternative therapeutic targets. Angiogenesis. 2017;20(4):409–26.
47. Pretzsch E, Bosch F, Renz B, Werner J, Angele M, Chaudry IH. Operative trauma and blood loss—impact on tumor growth and recurrence. Shock. 2021;55(4):455–64.
48. Bhamidipati CM, Coselli JS, LeMaire SA. BioGlue in 2011: what is its role in cardiac surgery? J Extra Corpor Technol. 2012;44(1):P6–12.
49. Alston SM, Solen KA, Sukavaneshvar S, Mohammad SF. In vivo efficacy of a new autologous fibrin sealant. J Surg Res. 2008;146(1):143–8.
50. Long M, Zhang Y, Huang P, Chang S, Hu Y, Yang Q, Mao L, Yang H. Emerging nanoclay composite for effective hemostasis. Adv Funct Mater. 2018. https://doi.org/10.1002/adfm.201704452.

Publisher's Note